

Basement structures from satellite-derived gravity field: South China Sea ridge

Carla Braitenberg,¹ Susann Wienecke,^{1,2,3} and Yong Wang⁴

Received 12 July 2005; revised 31 October 2005; accepted 4 January 2006; published 16 May 2006.

[1] The satellite-derived gravity over the South China Sea reveals high spatial frequency signals not present in the bathymetric models. The most evident is a linear feature of near 1000 km length, which parallels the South China Sea extinct spreading center. We formulate a crustal model of the South China Sea by constrained forward and inverse gravity modeling. The effect of the sediment layer is evaluated using the global sediment thickness model of NOAA and fitting the sediment compaction model to observed density values. The General Bathymetric Chart of the Oceans (GEBCO) and constraining data from seismology on crustal thickness are integrated in the inversion process, which includes the flexural isostasy model. The model crustal thickness values vary between 8 and 12 km and between 10 and 20 km over the oceanic and continental crustal part of the South China Sea, respectively. The elastic thickness is below 6 km over most of the sea, with lowest values in the margin (between 2 and 4 km). Finally, we invert the gravity data for the gravity-equivalent basement topography, which in sediment-covered areas corresponds to the basement and in sediment-free areas coincides with the bathymetry. We find a continuous ridge structure along the entire midbasin: It changes from a steep valley in the younger SW basin to a less pronounced valley in the NE basin, lined with seamounts. Our model shows the spreading center to be continuous and to bend from the older EW orientation to the younger SW-NE orientation rather than being made up of two separate axis segments.

Citation: Braitenberg, C., S. Wienecke, and Y. Wang (2006), Basement structures from satellite-derived gravity field: South China Sea ridge, *J. Geophys. Res.*, *111*, B05407, doi:10.1029/2005JB003938.

1. Introduction

[2] The knowledge of the basement in oceanic areas is of crucial interest in many applications of geosciences, as the basement, rather than the ocean bottom, is representative of the tectonic situation and history of a specific area. Because of sedimentation, a flat ocean bottom may hide a completely different tectonic situation of lineaments, tilted crustal blocks, ridges which affected the underlying basement. The structural elements of the basement can be useful in guiding the position and orientation of geophysical measurement campaigns aiming at investigating the crustal structure. In the special case of measurements carried out along profiles, it is optimal to trace profiles orthogonal to the structural lineaments. The basement not being globally charted, the ocean bottom topography must be used, which can be very misleading. Another example concerns the interpretation of magnetic anomalies over oceanic areas in

terms of the magnetic anomaly states. Where the magnetic anomalies are straight and well aligned, it is relatively straightforward to pick the paleomagnetic inversions along each magnetic anomaly profile. Greater difficulties appear in places where the anomalies bend or where two distinct directionalities meet. In this case the basement may reflect the direction of former spreading. Even some indication on the spreading rates can be qualitatively identified by inspection of the basement, by the fact that fast spreading ridges create relatively flat basement, with respect to slow spreading ridges [Kearey and Vine, 1996]. Also the identification of ridge segments dislocated by transform faults can be of great help or even essential in following the magnetic isolines. Another application is found in using the principle of isostatic balance and the observed gravity field in determining the lateral density or thickness variations of the lithosphere [Ebbing *et al.*, 2006]. In this case the estimation of the crustal loads is necessary, which are greatly determined by ocean water depth, basement depth, crustal thickness and the respective densities. Once the thicknesses and densities of these different layers are known, the loading can be calculated as well as the gravity field and the isostatic conditions. Deviations from equilibrium and residual gravity anomalies point to density anomalies in or below the crust. These in turn can be compared to seismic tomographic models revealing lithospheric velocity anomalies.

¹Department of Earth Sciences, Trieste University, Trieste, Italy.

²On leave from Institut für Geologische Wissenschaften, Geophysik, Freie Universität Berlin, Berlin, Germany.

³Now at Geological Survey of Norway, Trondheim, Norway.

⁴Institute of Geodesy and Geophysics, Chinese Academy of Sciences, Wuhan, China.

[3] Satellite-derived gravity data offers a good basis to undertake large-scale studies of regional crustal structure due to its global availability and its good quality. Over oceanic areas the short-wavelength component of the observed signal is generally well correlated with the bathymetry, a fact which was used by *Sandwell and Smith* [2001] and *Smith and Sandwell* [1997] to formulate the global bathymetric model derived from the integration of the global gravity anomaly field and shipborne bathymetric estimations. A comprehensive review of the different techniques used in bathymetric modeling from gravity data is given in *Calmant and Baudry* [1996]. An example of using geoid data from the ERS-1 Geodetic Mission to compute ocean floor topography is given in *Ramillien and Cazenave* [1997]. These works are similar to the approach we have used, but have one relevant difference. In fact, the gravity signal is nulled, where the inverted bathymetry does not correlate with the shipborne ocean bottom topography. The reason that the inverted signal contains more signal than the shipborne bathymetry, is due to the sedimentary blanket which covers the basement and reduces the amplitude of the ocean bottom features. It follows, that where the igneous basement is concealed by a sediment cover, the gravity anomaly may contain a high spatial frequency signal corresponding to the morphology of the buried basement. Such signals will not correlate with the bathymetry derived from actual ocean bottom depth measurements. When inverting the gravity signal for the ocean bottom, the information contained in the gravity field is only used partially, dismissing a considerable amount of the signal, which can be used for modeling the underlying structure.

[4] In oceanic areas the uppermost density discontinuities of the crust are (1) water surface, delimiting the atmosphere from the liquid ocean; (2) ocean floor, marking the transition from water to sandy, muddy or solid material, generally sediments; and (3) basement, marking the transition from oceanic sediments to consolidated rock. The ocean bottom is the bathymetry, and the undulation of the basement is the basement topography, a nomenclature we use for the remainder of the paper. For what concerns ship navigation and nautical mapping, exclusively the bathymetry is charted. The ocean bottom coincides with the basement topography only in places where the sedimentary cover is missing. The basement topography reflects the surface of great interest to the geoscientist, as to this surface all geologic and tectonic processes of the oceanic crust are frozen in. As time passes, these structures are slowly buried below the deposits of oceanic living and concealed to the observer studying the ocean bottom. For geologic studies, the basement topography underlying a sediment cover may be of great interest, in relating to tectonic features such as spreading axes, ridges, trenches and tilted crustal blocks. The interpretation of the gravity field in terms of the underlying structure can reveal important information in areas where seismic sounding is unavailable or to interpolate the structure between seismic profiles. A good example of such a situation is given in the South China Sea. The South China Sea has been generated by rifting and seafloor spreading, and the timing of the break up process has been reconstructed from the magnetic anomalies in the basin [*Taylor and Hayes*, 1980, 1983; *Briaais et al.*, 1993]. The timing found from the magnetic anomalies has been confirmed from the timing of extension

on the South China Shelf, at the northern margin of South China Sea [*Bellingham and White*, 2000; *Clift and Lin*, 2001; *Su et al.*, 1989]. The bathymetry does not reveal the morphology of the spreading axis, being nearly flat across most of the axis. Also the continental-ocean transition does not consistently coincide with any evident features in bathymetry. In contrast, the gravity anomalies clearly show the extinct spreading center, as well as the continental-ocean transition. Previous studies that mentioned the presence of a gravity signal in the South China Sea, attributable to the spreading axis, were made by *Hwang* [1999] and by *Wang et al.* [2001].

[5] In this paper we determine the basement and the CMI (crust-mantle interface) depth in oceanic areas from the combined analysis of the satellite gravity anomaly field, the bathymetric model, the sediment thickness model, data on the crustal thickness, and the application of the isostatic flexure model. As a by-product of our analysis we determine the isostatic state and the equivalent elastic thickness of the lithosphere. The main features of the gravity anomaly field and their relation to the opening of the South China Sea are discussed. A study of the loads on the crust and the resulting isostatic flexure and the implications on the gravity field follows. Last a model for the morphologic feature of the spreading center is presented and the results are discussed in the light of the hypotheses and implications obtained from the magnetic isochrons [*Briaais et al.*, 1993]. We investigate the structure of the South China Sea in this paper, but in principle the analysis could be extended also globally, with some requirements on the development of computational aspects.

2. Geological Outline of the South China Sea

[6] Figure 1 illustrates some bathymetric features of the South China Sea. The position of the spreading axis along the center of the basin is shown [after *Briaais et al.*, 1993]. The spreading and age has been determined from the observations of the magnetic isochrons in the basin [*Briaais et al.*, 1993; *Sibuet et al.*, 2004]. The shelf break lies between the isolines -200 m and -1000 m, and the -3000 m isoline is very close to the continent-ocean transition (dashed line). The spreading axis is divided into the E-W trending northern older segment (32–15.5 Ma) and the younger SW-NE trending segment (24–15.5 Ma). The basin is bounded to the north by the passive South China Sea continental margin, to the West by a postulated transform margin [*Nissen et al.*, 1995] and to the east by the Manila Trench (indented line), where oceanic crust is subducted under Luzon [*Nissen et al.*, 1995]. The Benioff zone of the South China Sea has been identified down to 140 km depth [*Lallemand et al.*, 2001]. The South China Sea slab has been postulated to extend as far as 660 km from the trench, and the subduction has commenced prior to 17 Ma [*Lallemand et al.*, 2001]. The age of the E-W trending magnetic lineations in the western basin have been estimated to correspond to ages 15.5–32 Ma, whereas the SW-NE trending lineations of the southwestern basin are younger and are estimated to be 15.5–24 Ma of age [*Briaais et al.*, 1993; *Taylor and Hayes*, 1983]. It can be concluded that the spreading of the basin extinguished 1–2 m.y. after commencement of the subduction process. According to

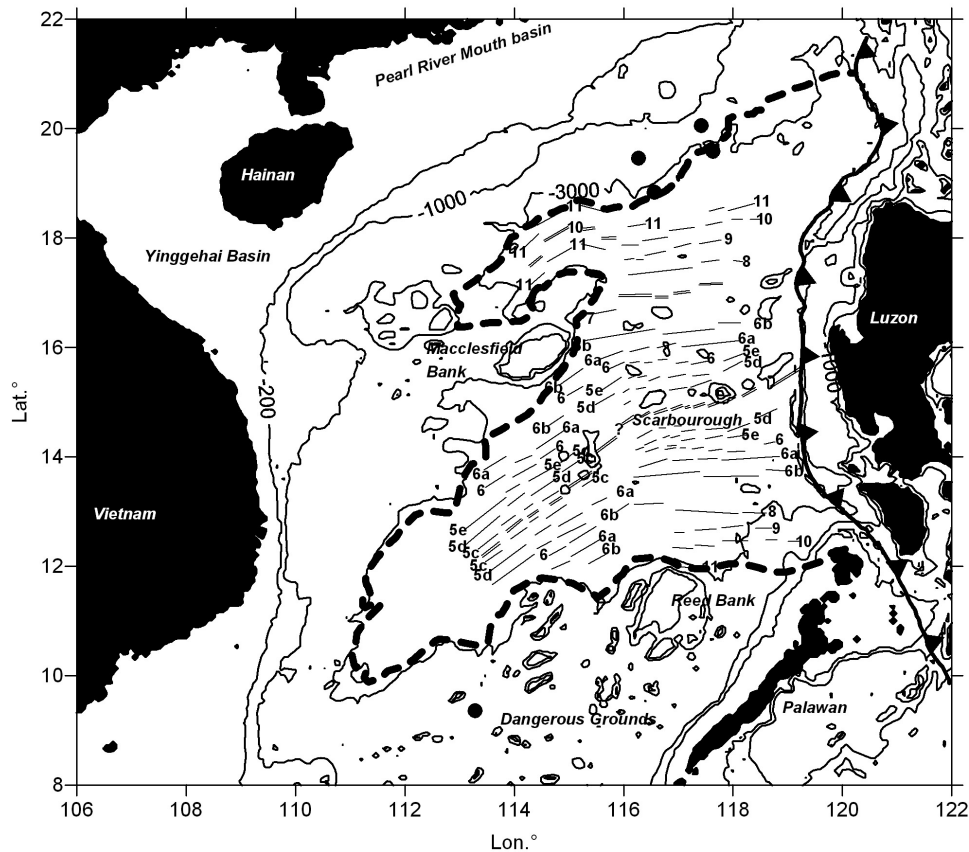


Figure 1. Bathymetric map of the South China Sea, with magnetic anomaly isolines according to *Briais et al.* [1993]. The double lines mark the spreading axis: the central spreading axis and the fossil spreading axis prior to the two southward axis jumps (see text). The continental-ocean transition is outlined as a dashed line. The bathymetric isolines for water depths 200, 1000, and 3000 m are shown, as they define the principal features that define the basin. The Manila Trench is also added [after *Ministry of Geology and Mineral Resources*, 1992]. Dots show positions of ODP drill sites.

Briais et al. [1993], in the eastern axial area seamounts were emplaced at 10–15 Ma, forming the Scarborough Seamount chain (Figure 1). The evolution of the South China Sea spreading center has been characterized by two southward ridge jumps, between anomalies 11 and 10 (32–30 Ma) and between anomalies 7 and 6b (26–24.5 Ma). The position of the fossil ridge is seen in Figure 1 with the two ridge segments near latitudes 18° and 17°. The ridge jump between anomaly 7 and 6b was accompanied by a rapid propagation of the ridge to the southwest. The spreading ceased in the southwestern sub basin (north of Macclesfield Bank) just after anomaly 10 (30 Ma). The ridge between anomaly 7 and 6b left an E-W trending fossil ridge just east of the Macclesfield Bank, extending from E116° to E118°. From the beginning of the oceanic spreading (32 Ma) to anomaly 5d (17.8 Ma), the spreading rate decreased from more than 60 mm/yr to about 35 mm/yr. It increased back to about 55 mm/yr between anomaly 5d and the cessation of spreading (15.5 Ma). It was not possible to reconstruct the spreading geometry in the zone around E115° because of poor magnetic data and a large number of seamounts. Here, according to *Briais et al.* [1993], a high-resolution study of the bathymetry of this area would be necessary. In the present study we show that this missing piece of information can be given from the gravity-equivalent

topography. The bathymetry does not give morphologic evidence of spreading because it is partly buried by a layer of sediments. The timing of the crustal stretching was studied by *Su et al.* [1989] and *Bellingham and White* [2000] on the northern margin of the SCS. The stratigraphic record of the Pearl River Mouth Basin was fitted by a two-dimensional (2-D) kinematic model. They find that modest amounts of rifting started at ~60 Ma, intensifying over the next 40 m.y., peaking at 20 Ma. The locus of maximum strain rate between 25 and 15 Ma is coeval with the opening of the southwestern SCS subbasin. *Clift et al.* [2002] have modeled the rifting process by studying the continental margins at conjugate positions using the flexural cantilever model of *Kusznir et al.* [1991]. Their model requires low elastic thickness of the lithosphere (below 10 km, flexural rigidity (D) below 9×10^{21} Nm) and they postulate lower crustal flow, in order to account for the observed subsidence, a further indication of a weak crust. They find indications that the elastic thickness for the South China margin is 1–3 km and slightly higher (8–10 km) for the Dangerous Grounds, which form the conjugate margin to the south of the basin. The study confirmed the conclusions drawn by *Clift and Lin* [2001] for the South China Shelf, where they had found isostatic compensation during crustal extension is close to being local. Here the one-

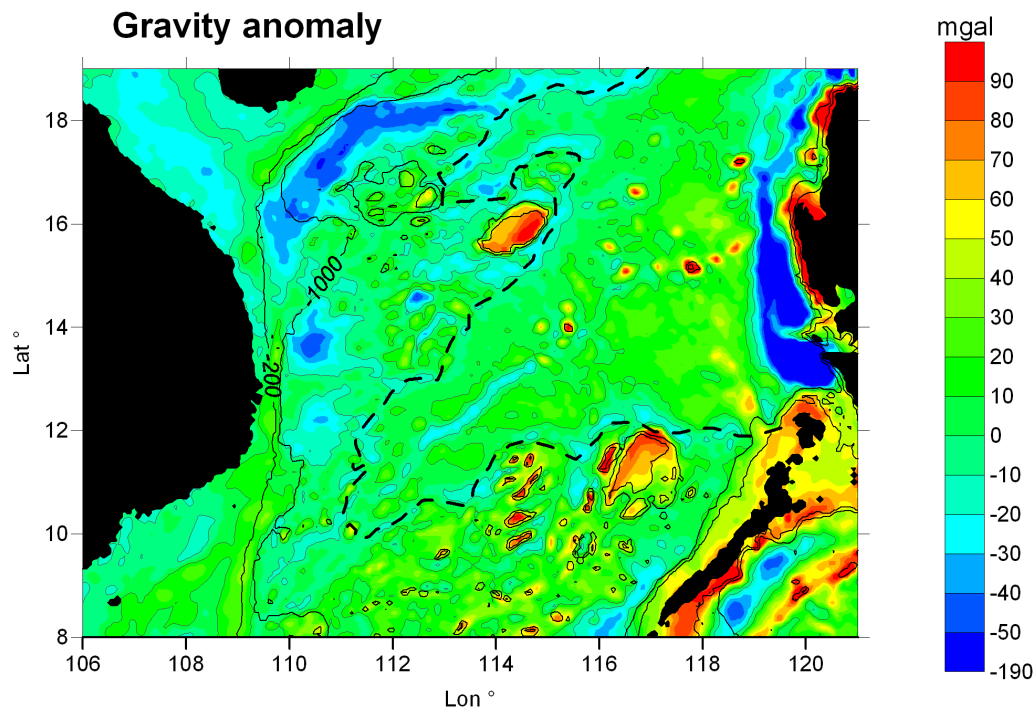


Figure 2. Observed satellite-derived gravity anomaly (gravity field after *Hwang et al.* [1998]). The continental-ocean transition is outlined as a dashed line, and the bathymetric isolines for water depths 200 and 1000 m are shown. The gravity anomaly isolines are traced for -20 and $+20$ mgal.

dimensional backstripping modeling technique was applied to drilling data for two basins, in order to calculate subsidence rates and the timing, amount and depth dependence of extension.

3. Data Sets

[7] Our study is based on gravity data, bathymetry measurements, sediment thickness and seismic crustal thickness evaluation. The studied area comprises the South China Sea, in an area defined in latitude by the interval $8-19^{\circ}\text{N}$ and in longitude by $105-122^{\circ}\text{E}$. We use the global satellite-derived gravity grid of *Hwang et al.* [1998]. The accuracies of the satellite-derived gravity field range globally between 3 and 14 mgal, as obtained from comparison with ship track gravity [*Hwang et al.*, 2002]. The accuracy is best over the deep sea and worst in the coastal areas (within 100 km from the coast) and over shallow seas, with depths less than 200 m [*Hwang et al.*, 2004]. For the specific case of the South China Sea, the RMS (root mean square) difference with the ship track gravity is 8 mgal [*Hwang et al.*, 2002]. The observed gravity anomaly is shown in Figure 2, and the land areas are marked in black. For orientation, again the -200 m and -1000 m bathymetric isolines are added, between which the shelf break lays. The satellite-derived gravity field with $2' \times 2'$ sampling of *Hwang et al.* [1998] was resampled at 4 km grid interval (we use Gauss Krüger projection, but another projection for example as UTM would lead to exactly the same results). The most evident feature is given by the negative gravity values along the extinct spreading center. Isolated bright spots are due to seamounts or small features emerging

above the basin. The Macclesfield Bank and the Reed Bank have positive gravity values up to 90 mgal. A segment of the shelf break south of Hainan Island has an elongated shaped negative gravity anomaly with values between $+20$ and -40 mgal. The continental-ocean transition is lined by a narrow negative gravity anomaly of about -20 mgal, of which we give evidence with the two isolines of -10 and -20 mgal on the map (gray isolines). The Manila Trench is marked by strongly negative gravity values. We use the bathymetry grid extracted from the GEBCO (General Bathymetric Chart of the Oceans) Digital Atlas published by the British Oceanographic Data Centre on behalf of IOC (International Oceanographic Commission of UNESCO) and IHO (International Hydrographic Organization) [*Intergovernmental Oceanographic Commission, International Hydrographic Organization, and British Oceanographic Data Centre (IOC, IHO, and BODC)*, 2003]. This grid has originally a resolution of 1 by 1 arc min and was resampled in the same way as the gravity data (Figure 3). In a first approach to our study we used the ETOPO5 bathymetry grid [*Braitenberg et al.*, 2004], which though has a smaller spatial resolution with respect to the GEBCO grid and therefore was not preferable in this study. For our purpose it is not possible to take the data from the widely used *Sandwell and Smith* [2001] bathymetric grid, as it is made with the use of satellite gravity data.

[8] The sediment thickness model was taken from the “Total Sediment Thickness of the World’s Oceans and Marginal Seas, World Data Center for Marine Geology and Geophysics, Boulder”. Presently this source was the only one publicly available. The digital total sediment thickness database was compiled by the National Geophys-

Topography/Bathymetry

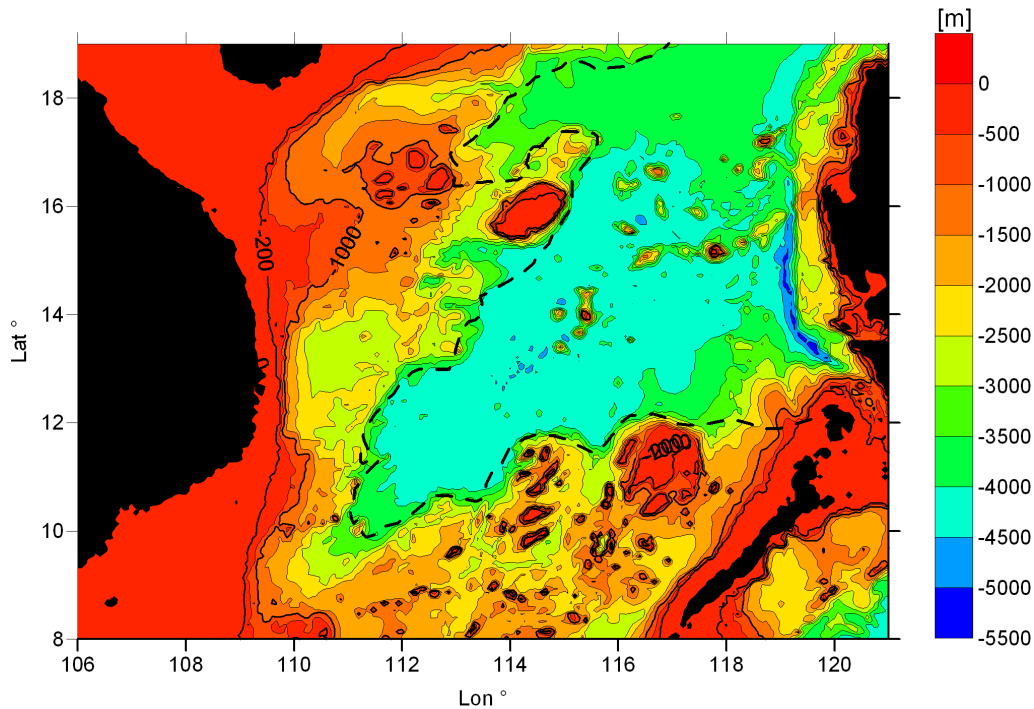


Figure 3. Map of the bathymetry grid released by GEBCO [IOC, IHO, and BODC, 2003]. The continental-ocean transition is outlined as a dashed line.

ical Data Center (NGDC) of NOAA (National Oceanic and Atmospheric Administration) and has a resolution of 5×5 arc min. The gridded data estimate the total sediment thickness, in meters, from the seafloor to the top of acoustic basement. Basement is presumed to be oceanic basaltic crust created at mid-ocean ridges. In some areas, however, strongly reflective chert layers and mid plate volcanic rocks mask the underlying oceanic crust. Therefore the deepest observable reflector in the seismic reflection profiles is defined as acoustic basement. It should be noted that acoustic basement might not actually represent the base of the sediments. These data are intended to provide a minimum value for the thickness of the sediment in a particular geographic region. Velocity regression equations were used to convert two-way reflection time, obtained from the seismic profiles, to thickness in meters. The sediment thickness for the South China Sea relied on the publication Ludwig and Houtz [1979]. In order to recover the corresponding sediment densities we have considered the drilling logs of ODP (Ocean Drilling Program) Leg 184 [Wang *et al.*, 2000], which comprises ODP Sites 1144–1148 for the northern margin and ODP Site 1143 for the southern margin of the basin. The cores are drilled at water depths ranging from 2047 m to 3305 m. Other data we used for our model include crustal thickness values that were available from Xu *et al.* [1997] and Nissen *et al.* [1995], from seismic refraction investigations.

4. Methodology

[9] The short-wavelength part of the gravity field over oceanic areas has been used with great success to formulate a

global bathymetric model [e.g., Smith and Sandwell, 1997; Sandwell and Smith, 2001]. This is particularly useful where the direct measurements of bathymetry are not publicly available or have not been fulfilled. During the inversion process of the gravity data, the main goal is the recovery of the bathymetry which should be as close as possible to the one recovered by direct measurement. For this purpose the gravity signal is nulled in the presence of a thick sediment cover, which buries the basement structures. In the study we have undertaken, the goal is the recovery of the basement structure, whether it is buried below sediments or coinciding with the bathymetry obtainable by direct measurement. In order to reach our goal, we therefore propose a methodology that makes use of the entire gravity signal and combines gravity inversion with flexural analysis.

[10] One standard approach is that of refining a starting bathymetry with means of the gravity data [e.g., Sandwell and Smith, 2001; Hwang, 1999]. In detail this could be done by (1) correcting the gravity field for the gravity effect of starting bathymetry and the sediment model, (2) low-pass filtering the gravity residual under the hypothesis that the CMI contributes most of the long-wavelength gravity signal, and (3) inverting the high-pass filtered gravity residual for a correction of the starting bathymetry. This approach though bears a few problems, which are overcome by the methodology we propose: (1) possible problems or errors of the bathymetric model, which can be present in remote or poorly explored areas directly enter the final result; (2) there is no control on the correctness of the hypothesis that the long-wavelength field is due to the CMI; (3) there is no control on the adequateness of the CMI, and existing data from seismic investigations on the depth of the CMI are not taken into account.

[11] The methodology we propose operates in the frame of a complete physical model, which considers the load of bathymetry and sediments and includes all available refraction seismic data on the depth of the CMI. Therefore much greater control is possible on the portion of the gravity field ascribed to be due to the CMI than by simple low-pass frequency filtering.

[12] The approach we use in the inversion of the crustal structure and of the flexural rigidity involves a series of steps, which include (A1) a gravity inversion and (A2) calculation of the flexure of the crust beneath the topographic and intracrustal load. Then we calculate the gravity field due to the crustal thickness variation (A3) and the inversion of the residual gravity, obtained by correcting the observed gravity anomaly for the crustal thickness variations and the sediment cover (A4). The starting point of the analysis is the database containing gravity observations, crustal thickness estimates from seismic investigations, the total sedimentary thickness, and a bathymetry/topography model.

4.1. Step A1

[13] The first part of the work models the CMI depth variations. Because of the $1/r$ dependence (r distance from observer to mass point) of the gravity potential field, the short-wavelength variations of the gravity field are filtered out greatly with increasing distance from the mass source [e.g., *Zadro*, 1986; *Blakely*, 1995]. It follows that the long-wavelength part of the observed gravity field is generated by CMI undulations, the short-wavelength part being due to the superficial masses. This does not exclude that also the superficial masses contribute to the long-wavelength part of the field. For the CMI undulations to be inverted from the gravity data, the gravity values are corrected for known masses, that is, the bathymetry (Bouguer correction) and the sediment thickness variations. The residual field is inverted by applying iterative constrained inverse modeling [*Braitenberg et al.*, 1997]. At present we have no constraints on lateral density variations in the lower crust, so that a constant density contrast across the interface must be assumed. We will discuss below, to what extent the results may be altered by a possible density variation. The method has been extensively tested on synthetic models [*Braitenberg and Zadro*, 1999] and in various geographical areas such as Alps and Tibetan Plateau [*Braitenberg et al.*, 1997, 2000, 2002, 2003; *Zadro and Braitenberg*, 1997; *Ebbing et al.*, 2001]. The method requires some starting parameters, including the reference depth of the density interface (d) and the density contrast across the interface ($\Delta\rho$). Furthermore, the cutoff wavelength that limits the wave number range used in the inversion must be set. The CMI depth estimates from seismic investigations are used as constraints for the choice of the two relevant parameters d and $\Delta\rho$.

4.2. Step A2

[14] The next modeling step involves flexure [*Watts*, 2001], which is an independent means to determine the CMI undulations and allows the gravity-deduced CMI undulations to be checked for consistency. The modeling of the CMI undulations in terms of the thin plate flexure model is done by a least squares approximation of the gravity CMI evaluated in step A1 of the procedure. The

flexure is calculated by the convolution of the crustal load with the point-load flexure response curves, as described by *Braitenberg et al.* [2002, 2003]. A set of flexure response curves were prepared, pertaining to the elastic thicknesses ranging from $T_e = 0$ km to $T_e = 25$ km at a step of 0.5 km. The convolution radius varies in function of the elastic thickness between 25 and 270 km. Greater elastic thickness values require a greater convolution radius. We refer to the discussion and the tests published by *Braitenberg et al.* [2002, 2003] on the optimal choice of the convolution radius. The convolution method is superior with respect to spectral approaches in the recovery of the spatial variation of elastic thickness: the tests performed on the recovery of the elastic thickness values of a synthetic model have shown that the elastic thickness can be calculated on square windows with side lengths as small as 100 km [*Braitenberg et al.*, 2002]. In fact, on square windows of side length L the difference between the gravity CMI and flexure CMI may be calculated. The RMS difference between the two undulating surfaces is minimized by varying the elastic thickness T_e . The result is a solution of the flexed crust that is in best agreement with the long-wavelength component of the gravity field. It gives a physical model of the CMI on the basis of the theory of flexural isostasy, in contrast to the CMI obtained in step A1, which is based on the spectral analysis of the observed gravity field.

4.3. Step A3

[15] The purpose of the third step is to isolate the observed gravity anomaly from the gravity signal of the CMI and from the sediments. The gravity effect of the CMI is calculated with a constant density contrast across the CMI, calculating the gravity effect by application of the Parker algorithm [*Parker*, 1972]. This resulting field (g_{CMI}) and the gravity field due to the sediments (g_{sed}) are subtracted from the gravity anomaly:

$$g_{\text{res}} = g_{\text{obs}} - g_{\text{CMI}} - g_{\text{sed}} \quad (1)$$

[16] Here the flexural CMI (calculated in step 2) is used, because it is based on a physical model. We will show later, that the difference between the flexure and gravity CMI is quite small (less than one km) over most of the basin, so that the final result is not affected by using either one of the CMIs.

4.4. Step A4

[17] In the last step the gravity-equivalent basement topography is calculated. This is done by inversion of the field g_{res} . The diagram displayed in Figure 4 summarizes the four steps discussed above. The inversion made in Step A1 is by the iterative constrained inverse modeling. In the ideal case, the residual gravity represents the field of the basement topography, having been freed from the gravity field generated by the sediments and the CMI. This residual field contains both high-frequency and low-frequency spectral contents of the gravity field generated by the basement topography. The inversion process can be made on a single reference depth, without the necessity of inverting on a series of depth levels as is required in the case that the gravity anomaly is used for correcting a starting bathymetry [e.g., *Hwang*, 1999]. When inverting for the ocean bottom

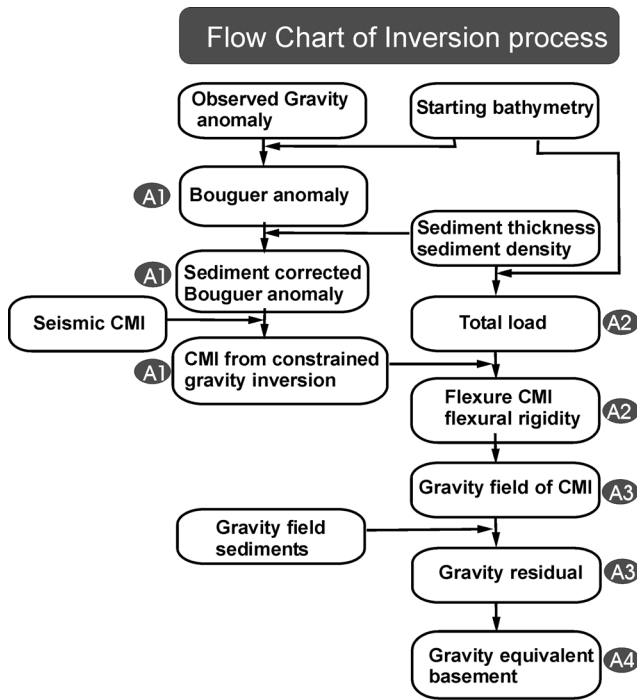


Figure 4. Flowchart illustrating the different steps of the modeling and inversion procedure. A1 to A4 refer to the steps explained in section 4.

from the gravity signal, we must use the density contrast between crust and water. In order to be able to use this same density difference also for the inversion of the basement, the sediments-gravity effect must be calculated against the

reference density of water. The sediments can be regarded as a surplus mass relative to water. The reference depth in this case is set to zero level.

5. CMI Inversion and the Gravity-Equivalent Basement Topography

[18] The gravity-equivalent basement topography is calculated following the steps explained above and is illustrated in Figure 4. Step A1 involves correcting the gravity field for the effect of the sedimentary cover. The sediment model of the South China Sea furnished by NOAA consists of sediment thickness only (Figure 5), so the density must be obtained from other source. Direct density measurements exist for the Ocean Drilling Program (ODP) cores taken from the South China margin [Wang *et al.*, 1997]. The values taken from ODP cores are limited to a maximum sub-sea floor depth of 800 m. We compare the data with the sediment compaction model of *Sclater and Christie* [1980], which is based on an exponential reduction of porosity with depth. With ρ_g the grain density, ρ_f the fluid density, φ_0 the starting porosity and d the depth decay parameter, the density in dependence of the depth below seafloor (z) is calculated as

$$\rho(z) = \rho_f \varphi_0 e^{-z/d} + \rho_g (1 - \varphi_0 e^{-z/d}) \quad (2)$$

The observed density values are well fitted with the parameters $\rho_f = 1030 \text{ kg/m}^3$, $\rho_g = 2800 \text{ kg/m}^3$, $\varphi_0 = 0.8$ and $d = 1.5 \text{ km}$. The exponential compaction model was used by *Su et al.* [1989] to model the porosity variation with depth in the northern margin of the South China Sea. These

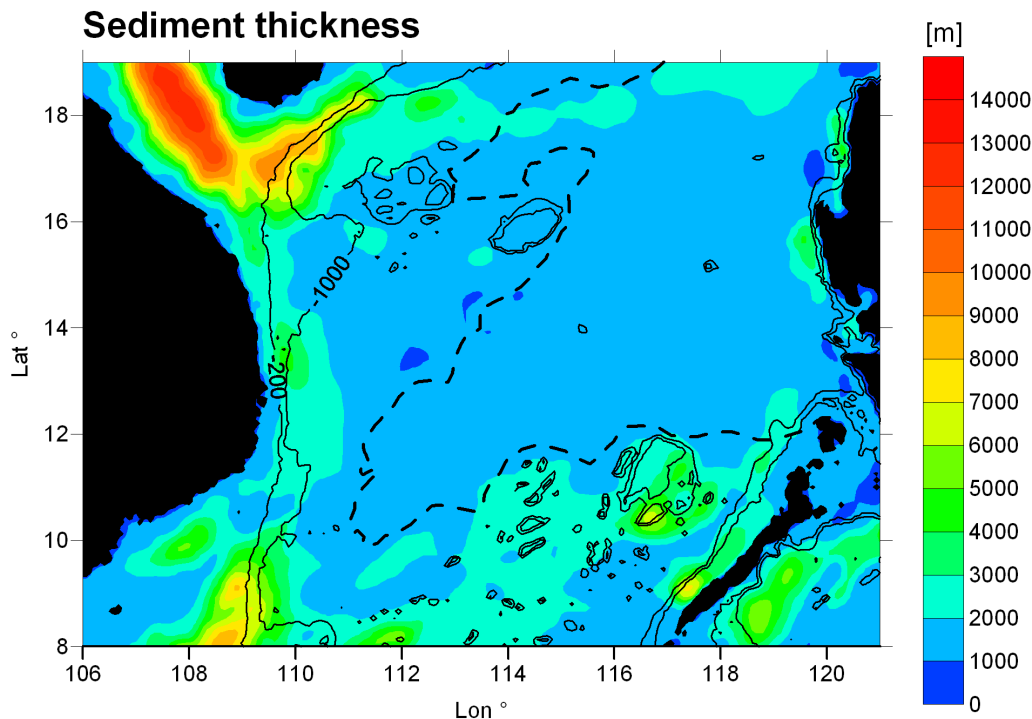


Figure 5. Model of sediment thickness according to the grid compiled by NGDC (see text for more details on the sediment model). The continental-ocean transition is outlined as a dashed line, and the bathymetric isolines for water depths 200 and 1000 m are shown.

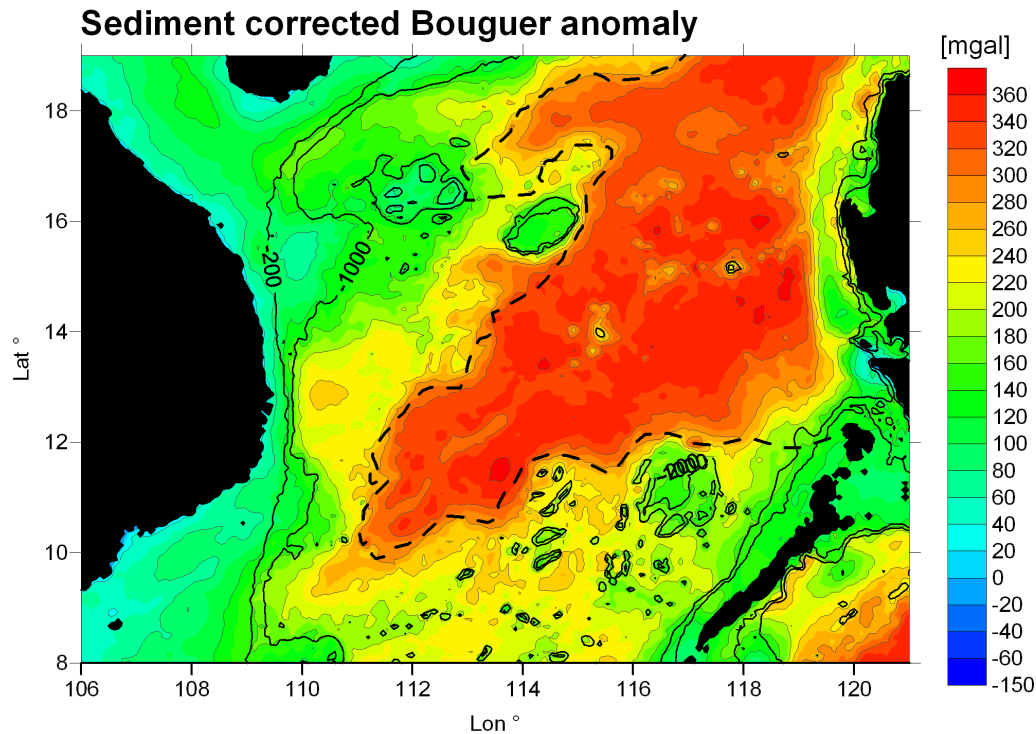


Figure 6. Bouguer anomaly field corrected for sedimentary cover. This field is used for the constrained inversion of the crust-mantle interface. The continental-ocean transition is outlined as a dashed line, and the bathymetric isolines for water depths 200 and 1000 m are shown. The Bouguer anomaly isolines are traced at 40 mgal intervals.

parameters are consistent with the drilling results of ODP, where the highest porosity is 0.8 for all six sites, and the grain density is between $2700\text{--}2800\text{ kg/m}^3$ [Wang *et al.*, 2000]. The gravity effect of the sediments is calculated by dissecting the sediment model of *Sclater and Christie* [1980] with a series of thin sheets (10 m thickness) with laterally variable density, calculated with equation (2). The sediments contribute with a nonnegligible amount to the gravity signal: the deep Yinggehai Basin to the NW of the map gives a prominent signal of up to $-135 \times 10^{-5}\text{ m/s}^2$. The sediment corrected Bouguer field is displayed in Figure 6, which is the field used for the inversion of the CMI. Because of the lack of constraining data, we set a constant density contrast ($\Delta\rho$) across the CMI. We let the reference depth (d) and the density contrast vary within standard values of 20–30 km and $350\text{--}600\text{ kg/m}^3$, respectively. The gravity field is inverted for the different combinations of parameters and the root mean square (RMS) difference with the constraining values of CMI from seismic reflection data is calculated. The constraining values are given as labeled crosses in Figure 7. The best agreement (1.8 km rms) between the gravity-derived and seismically measured CMI depth is found for the couple of d and $\Delta\rho$ equal to 25 km, 530 kg/m^3 .

[19] The cutoff wavelength (P_{\min}) is estimated from the decay of the amplitude spectrum of the gravity field [e.g., *Russo and Speed*, 1994] and was found to be 120 km. In Figure 7 the depth to the CMI calculated from the gravity inversion is displayed. Below the South China Sea basin the CMI shallows to a depth of about 9 km, below the Dangerous Grounds it is of the order of 14 km, and it is

about 20 km deep below the South China margin. The eastern and western parts of the oceanic part of the basin are distinguished by particular depth variations of the CMI. We proceed now to test the compatibility of the CMI obtained from the constrained gravity inversion with the physical model of flexural isostasy (step A2). We first calculate the crustal load, which consists of the sum of the topographic load and the intracrustal load, the latter consisting of the sediments. Over oceanic areas the load is negative, as the water-filled basins are lighter than the reference crust. The same is true for the sediments, as long as the density is less than the crustal reference density. We apply the methodology introduced in *Braitenberg et al.* [2002, 2003] for the flexure analysis. The flexural rigidity is calculated on sliding square windows of 100 km side length, shifted by 20 km. We use standard parameters for the Young modulus ($E = 100\text{ GPa}$), the Poisson ratio (0.25) and mantle (3300 kg/m^3) and crustal density (2800 kg/m^3). The gravity CMI is in excellent agreement with the flexure model, as confirmed in Figure 8, where the difference between the flexural and gravity CMI is displayed. In general, the difference in CMI depth is small, around 1 km. The greatest differences are found along the Manila Trench, where the oceanic plate subducts under the Philippine Islands. Systematically the residuals tend to be negative to the northwest of the spreading axis and positive to the southeast. This is due to a long-wavelength positive gradient toward southeast in the gravity field, which induces a shallowing of the inverted gravity CMI. The elastic thickness variations are displayed in Figure 9. Over most of the South China Sea the elastic thickness is below 6 km. The continental crust west

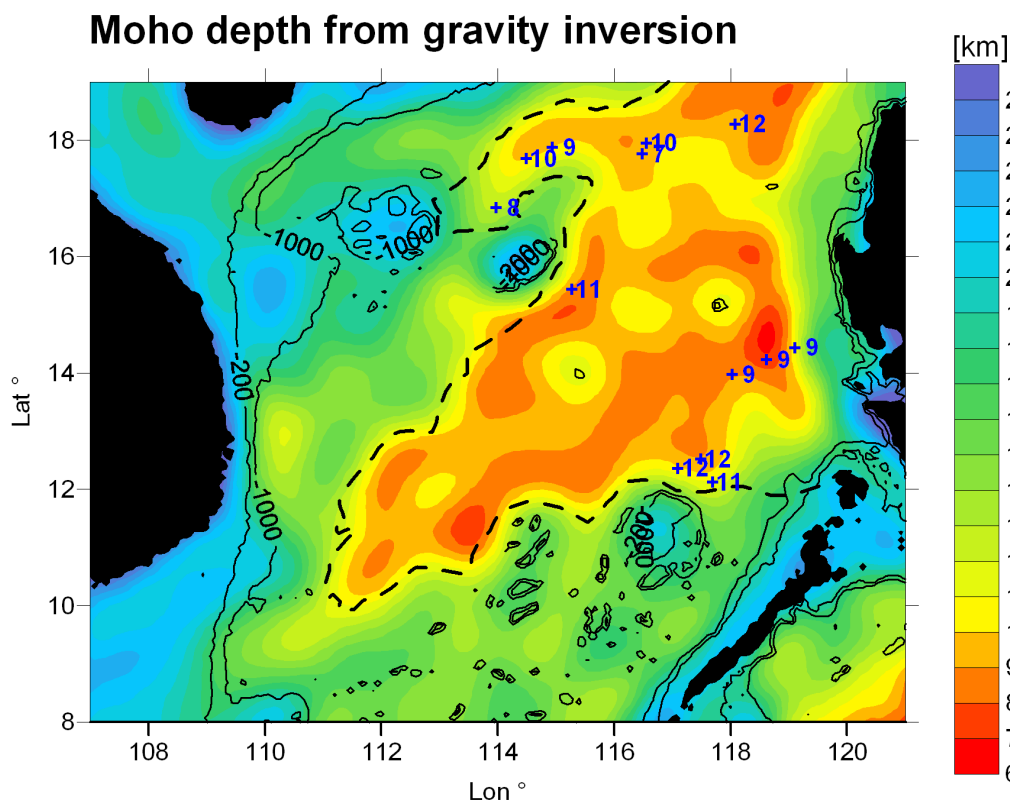


Figure 7. Map of the crust-mantle interface obtained from the constrained gravity inversion. Depths are calculated below sea level. This is termed the gravity CMI. The continental-ocean transition is outlined as a dashed line, and the bathymetric isolines for water depths 200 and 1000 m are shown. The CMI depths (km) from seismology are marked as labeled crosses.

of the South China continental-ocean transition has values between 2 and 4 km. The Dangerous Grounds have slightly higher values of 4–6 km. The South China shelf area has higher values, up to 14 km. The bathymetric high of the Reed Bank has a localized higher value of T_c (6–10 km). Anomalously high T_c values are found along the South China shelf break, where the gravity anomaly is characterized by low values (see previous discussion and Figure 2). In addition, we also found anomalously high T_c values along the southwestern segment of the extinct spreading axis (up to 20 km). We now calculate the gravity field of the CMI, and subtract it and the gravity field of the sediments from the gravity anomaly (step A3), obtaining the residual field (g_{res}) (equation (1)). We may now proceed with the last step in our analysis, concerning the inversion of the gravity residual. This step results in the gravity-equivalent basement topography. For the inversion we again pose a constant density contrast ($\Delta\rho_b$), and all wavelengths contained in the gravity field are taken into account. As the density contrast acts as a linear scaling parameter, any known values of the basement depth allow constraining the value. Alternatively we may rely on a standard value, bearing in mind that the density acts as a linear scaling parameter in the amplitudes of the basement topography. We adopted the density 1770 kg/m^3 that corresponds to the density contrast of crust to water, using the above crustal density of 2800 kg/m^3 and the water density 1030 kg/m^3 . The reference depth is set to zero. In Figure 10 the resulting

gravity-equivalent basement topography is graphed as contour lines, Figure 11 shows the same model as a 3-D relief, the inlay giving a zoom on the central part of the basin (corresponds to white box). Compared to the GEBCO bathymetry it presents a greater amount of small-scale features, of which the most evident is the linear ridge and graben along the spreading axis. Compared to the bathymetric model of *Smith and Sandwell* [1997], it has some similarities, the latter being also derived from an integration of the gravity field and the shipborne bathymetry. The magnetic anomaly isolines [*Briaies et al.*, 1993] have been added to Figure 11. The basement is either deeper or at the same depth as the bathymetry, depending on the sediment thickness. Where there are the deep basins of several km thickness, the basement is accordingly deeper than the ocean bottom. The ridge and graben structure we find in the center of the basin correlates along the greater part of the magnetically inferred younger southwestern segment and the eastern part of the older northeastern segment of the spreading axis. Concerning the transition zone of the two axis segments, the interpretation of the magnetic anomalies are in disagreement between different publications: according to the *Ministry of Geology and Mineral Resources* [1992], the spreading axis and magnetic anomalies have a gap in the transition zone; while according to *Briaies et al.* [1993], in the transition zone great uncertainties in the interpretation of the anomalies and identification of the isolines prevail, so it could not be decided whether the

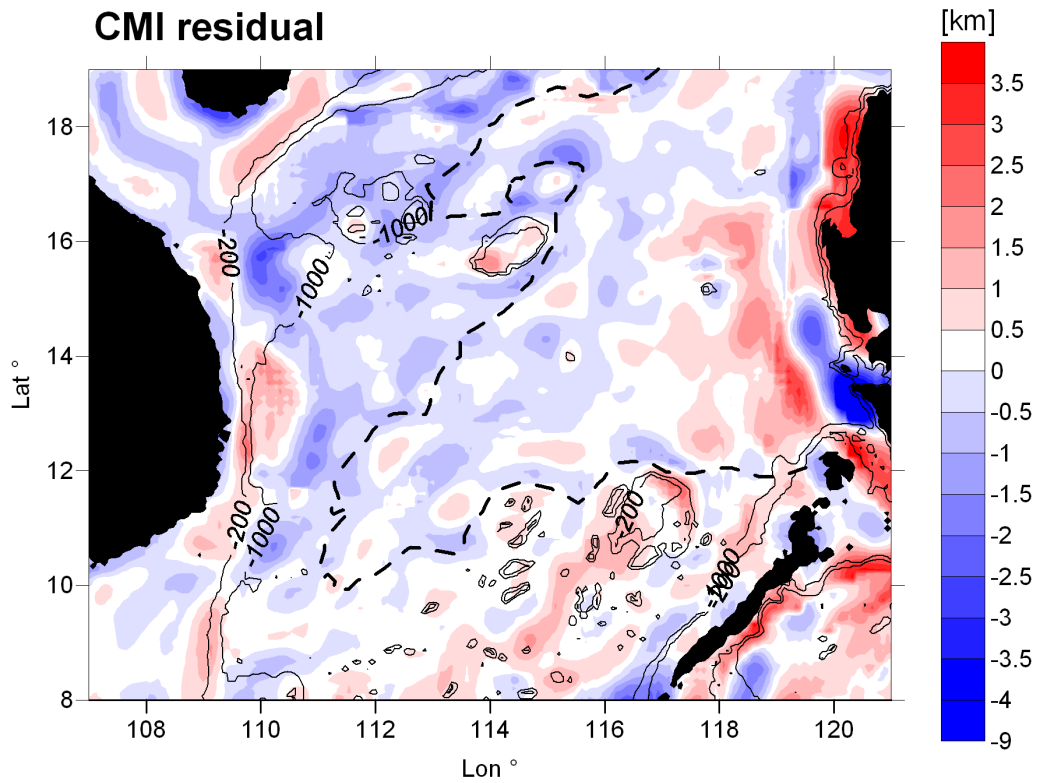


Figure 8. Difference between the CMI undulations obtained from gravity inversion and those obtained from the flexure model (km). For positive values, flexure CMI is shallower than the gravity CMI. The continental-ocean transition is outlined as a dashed line, and the bathymetric isolines for water depths 200 and 1000 m are shown.

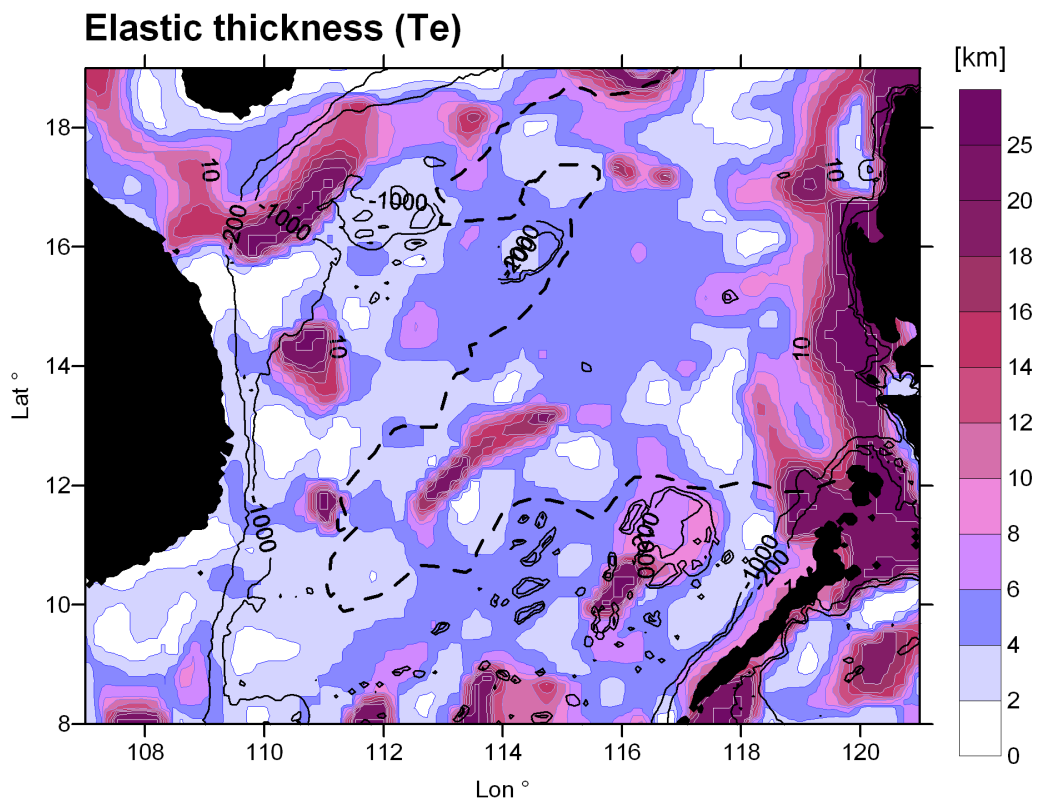


Figure 9. Elastic thickness (km) of the South China Sea. The continental-ocean transition is outlined as a dashed line, and the bathymetric isolines for water depths 200 and 1000 m are shown.

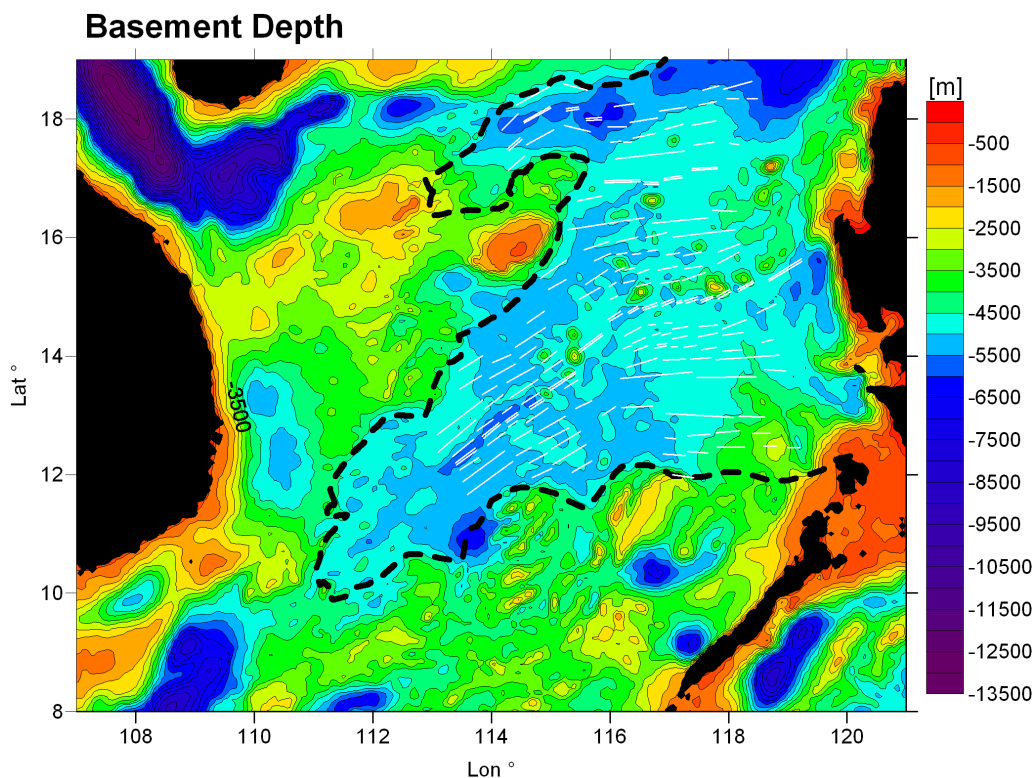


Figure 10. Basement depth from gravity inversion (colors represent isolines). The continental-ocean transition is outlined as a dashed line, and magnetic anomaly isolines (white lines) are given according to *Briais et al.* [1993].

eastern and western parts of the axis are disjunctive or connected. In the latter publication the entire axis is interpreted as consisting of dislocated ridge segments. However, our gravity-derived basement reveals a continuous ridge and graben structure, with an increase in the occurrence of seamounts toward the eastern basin; the gap in the transition zone is not seen, and a bend is observed that conducts from the E-W oriented older segment toward the SW-NE orientation of the younger segment of the axis. Also interesting is the shallowing of the basement along the fossil spreading axis in the northwestern subbasin. Here the ridge structure is broader and less evident with respect to the structure found along the central axis (see Figure 11).

6. Discussion

[20] In the study of the gravity anomaly field of the South China Sea we have found remarkable short-wavelength topographic features. Because of their short wavelengths, they must be generated by relatively shallow mass sources [e.g., *Spector and Grant, 1970; Blakely, 1995*]. Inspection of the bathymetry reveals that they are partly uncorrelated with existing models of the seafloor. The most evident of these is a 750 km long and 30 km wide linear gravity low with peak to bottom amplitude of about $30\text{--}50 \times 10^{-5} \text{ m/s}^2$, that follows the spreading axis, which was extinguished at 15.5 Ma [*Briais et al., 1993*]. We propose that this gravity signal is generated by basement topography now buried by sediments. In fact inspection of Figure 3 shows clearly that the shipborne seafloor topography is rather flat, apart from some seamounts. We have used the gravity signal to build a

gravity-equivalent basement topography that contains features buried by sediments such as the extinct spreading axis. The inversion procedure integrates all available data on the crustal structure, as seismically derived crustal thickness, the ODP scientific drill logs, the existing models of sediment thickness and the physical model of flexural isostasy.

[21] The accuracy of the basement model depends in its high-frequency part entirely on the gravity anomaly data. The long-wavelength component depends on several parameters, which are the long-wavelength component of the gravity field, the sediment model, and the gravity effect of the CMI. Worldwide, the satellite-derived gravity anomaly data have an accuracy that ranges from 3.0 to 13.4 mgal [*Hwang et al., 2002*], calculated from comparison with ship borne gravity data. In general, the large difference between the data sets may be due to (1) bad sea tide and sea currents correction and contamination of altimeter waveforms by landmass and reefs and (2) large gravity signatures due to trenches and seamounts. For the South China Sea the RMS difference compared to the ship borne gravity is 8.0 mgal [*Hwang et al., 2002*]. We expect this value to be affected by the second of the above mentioned problems, as problem (1) does not apply, because this is a deep and extended sea. Therefore, in areas of the South China Sea that are not seamounts or trenches, the accuracy can be expected to be better than 8 mgal, and as low as 3 mgal. Unfortunately it is unknown what the frequency dependency of the accuracy is, which would be essential if we are to estimate the derived accuracy of the inverted basement topography. The sediment model is completely flat in the oceanic basin and thus affects the basement topography only as a constant value,

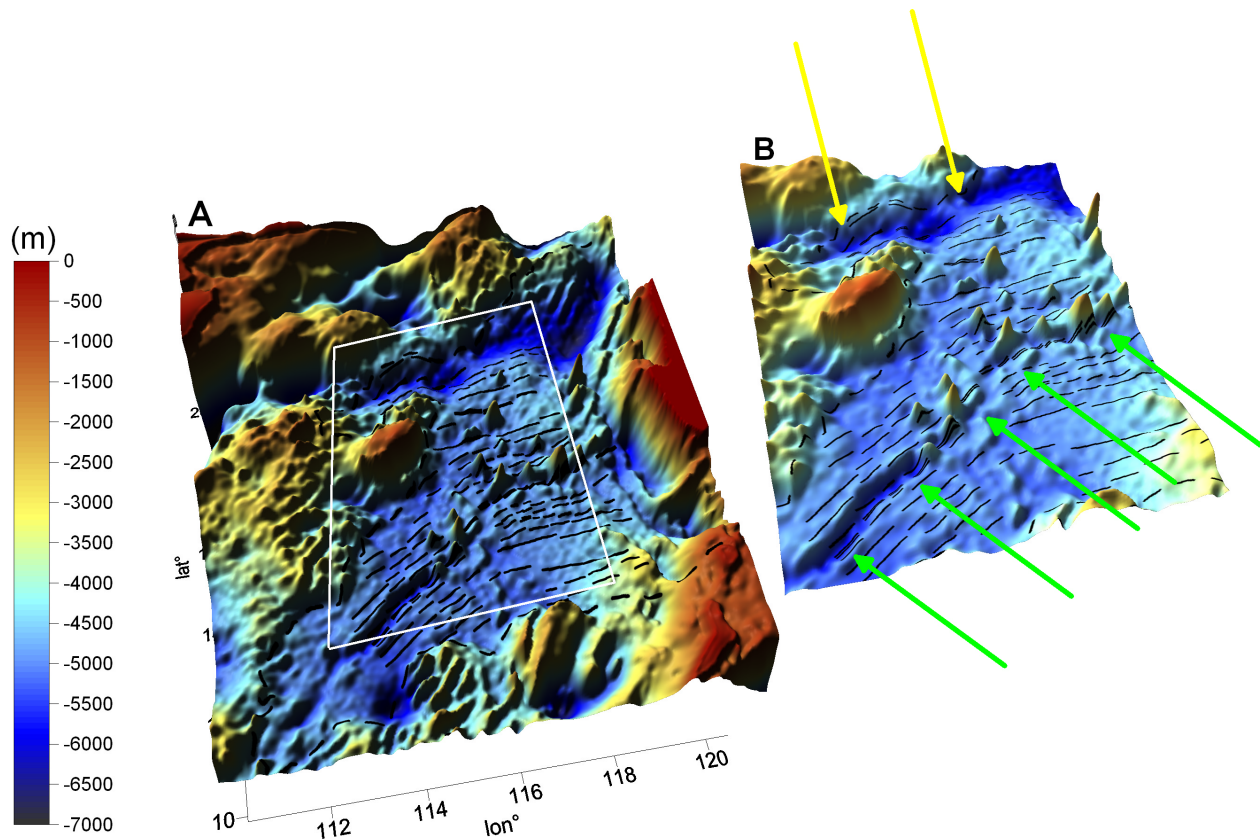


Figure 11. Basement depth from gravity inversion: color relief map of the basement model and zoom on the extinct spreading axis. The continental-ocean transition is outlined as a dashed line, and magnetic anomaly isolines (black lines) are given according to *Briais et al.* [1993]. Green arrows indicate the central spreading axis, and yellow arrows indicate the extinct spreading axis in the northwestern subbasin.

pushing the basement below the sediment layer. Features of the basement such as the spreading axis or the ruggedness over the stretched continental crust are mostly unaffected by possible problems in the sediment model. The basement topography is strongly dependent on the sediment model below the deep sediment basins on the South China shelf area, west and south of Hainan Island, and in the area of the Dangerous Grounds. The wavelengths of the basement that are affected by the sediment model are in the order of 200–400 km. In general, consideration of the sediment model introduces long-wavelength (200–400 km) features into the basement model, that are not necessarily contained in the gravity anomaly observations. Neglecting the sediments has the effect of underestimating the basement depth. Nonetheless, short-wavelength features of the basement can be recovered from the gravity data without taking into account the sediment model, in areas where the latter is unavailable.

[22] One result of the study is a model of the CMI undulations which obeys the flexural isostatic theory and is a best fit to the seismic constraining CMI depths and the gravity field. Because of the lack of constraining data on the density variations at the base of the crust, we have used a laterally constant density contrast. The density contrast acts as a linear scaling parameter to the undulations of the CMI with respect to the reference depth. When more constraining data are available, the variable density contrast can be used

to make a correction to the CMI model. If the real density contrast were smaller (or greater) than the one we assumed in the inversion, the deviation of the CMI from the reference depth would result in its depth being underestimated (or overestimated). Taking the central South China Sea basin as an example, the real density contrast across the CMI being 10% less (greater) than the value used (530 kg/m^3) would imply a shallowing (deepening) of the CMI by 1.5 km. On the margin, where the CMI is nearer to the reference depth, the shallowing (deepening) would be in the order of 0.5 km.

[23] Along the active subduction margin to the east of the South China Sea basin, we predict that the flexural isostatic model would be influenced by the stresses of the down-going plate. In fact in this area we find the greatest deviations between the flexure CMI and the gravity CMI. A specific analysis focusing on this problem would go beyond the scope of the present paper. We therefore pose a caveat for the CMI model in the subduction influenced area. The CMI responds isostatically to the bathymetry, in the sense that the deep basin (e.g., $>4000 \text{ m}$) is underlain by a thin crust of 9 km thickness. The gravity anomaly values oscillate around the zero value, which is an indication of the fact that the isostatic equilibrium is achieved. We may compare our results with existing CMI models as [*Lebedev and Nolet*, 2003; *Bassin et al.*, 2000]. These have a lower resolution (400 km and 2 degrees, respectively), so the

comparison can be fulfilled only regionally. Our model is in better agreement with the crustal thickness model of *Bassin et al.* [2000], as the model of *Lebedev and Nolet* [2003] contains a deepening of the CMI down to about 30 km in the southwestern basin, which we do not obtain.

[24] The elastic thickness values (T_e) over most of the basin are below 6 km. There are no considerable differences in elastic thickness between the oceanic and continental stretched crust. For rifts where extension exceeded 30%, as is the case in the South China Sea [*Clift et al.*, 2002], *White* [1999] noted that the elastic thickness ranged from 1 to 11 km, with a mode of 5–6 km. The value we find complies with this study. The higher value of T_e (up to 14 km) under the South China shelf is similar to what *Lin and Watts* [2002] estimated from a study of the flexure of the eastern edge of the Chinese margin under the Taiwan fold and thrust belt. *Clift et al.* [2002] estimated the elastic thickness for the Dangerous Grounds from the study of the width of the flexural trough, yielding a value of about 8–10 km, which is only slightly higher compared to our value of 4–6 km. As explained above, the T_e solutions along the active subduction margin of the South China Sea (Manila Trench) may be distorted, as the simple flexural model is a simplification. In fact here a more complete model must be used that considers the stresses tied to the subduction process.

7. Conclusion

[25] The basement is crucial in identifying tectonic features and constructing the tectonic and geodynamic history of oceanic areas. Basement which has been unaffected by tectonic events over the recent geologic history, has nonetheless seen continuous sedimentation, resulting in a steady process working at concealing and burying morphologic features. With increasing time since emplacement, the amplitude above seafloor of the tectonic features such as seamounts, ridges and tilted blocks will steadily decrease. Steep features of low amplitude will be the first ones to disappear, distorting the tectonic framework. The topics that are affected by this problem are manifold, as for instance the study of plate tectonic movement from hot spot traces, the statistics of seamount populations and the interpretation of magnetic anomalies over oceanic areas in terms of the magnetic anomaly stage. As seen in our example of the SCS, the structural features related to the extinct spreading axis are greatly concealed below a sediment blanket and therefore not seen in the ocean floor. The estimated basement depths are important input parameters for further investigation of the time evolution of the overlying sediments. The provided basement depths are crucial for the investigation of the temperature distribution within the sediments above. Since the temperature of any stratum as a function of depth and time can be used for calculation of the oil window [*Su et al.*, 1989], the estimated depths of the basement are crucial for the investigation of the hydrocarbon maturation in the sediments.

[26] We have shown that it is possible to give a 3-D model of the basement globally over oceanic areas. Necessary input data are the satellite-derived gravity field, the bathymetry, the sediment thickness, and the lithospheric flexure model of regional isostasy. We have chosen the SCS as an example for our calculations. The SCS formed by

seafloor spreading, which ceased at 15.5 Ma, after which seamounts were emplaced. Compared to the gravity field, the ocean bottom is flat, an indication of the fact that the tectonic features have been buried below sediments. Analogous situations in other areas of the world could be found by forming the coherence between the gravity anomaly and the bathymetry. In places where the coherence is low, our method could be used to extract concealed features of the basement.

[27] In our application of the SCS, we find that the morphology of the spreading center changes along its axis: in the southernmost part it is a deep trough lined by high shoulders (rift and graben structure), toward the older part to the north, this graben structure is less pronounced. Characteristic of the northern, older spreading center is the abundance of seamounts, nearly missing in the southwestern part. A cluster of seamounts is found at the intersection of the line connecting the conjugate Macclesfield Bank and Reed Bank and the spreading axis. An elevated linear feature in the basement connects the two banks. Presently we lack information on the age and composition of the conjugate banks. The linear feature could be explained as having been produced by an increased magmatic generation, which also produced the cluster of seamounts after spreading ceased, or shortly before it stopped. The fact that an alignment of seamounts connecting the two Banks is not found indicates that the source alternated productive with quiescent phases. We find continuity in the ridge and graben structure in the transition zone from the SW-NE trending to the E-W trending segments of the spreading center, where the two segments are connected by an S-shaped bend. This continuity gives new perspectives to the interpretation of the magnetic seafloor anomalies. In particular to what extent the identification of the anomalies on both sides of the spreading axis along the central part of the axis are really good, where greatest uncertainties are present in the magnetic picking [*Briais et al.*, 1993]. It is interesting to interpret our results in the context of the findings of the MELT experiment designed to investigate structure of mid-ocean ridges [*Forsyth et al.*, 1998]. As along the East Pacific Rise, which was the object of the MELT experiment, the South China Sea seamounts are distributed asymmetrically along the spreading axis, the population being greater on the northwestern side compared to the southeastern side. In contrast to the East Pacific Rise, the ridge jumps have been in opposite direction (southward) with respect to the side of greater population of seamounts. From the distance between the magnetic isolines no asymmetry in the spreading rates can be inferred. At Moho level symmetry across the spreading axis is observed, with local isostatic deepening below the greater seamounts or clusters of seamounts. The gravity field has a long-wavelength component with lower values to the northwest of the spreading axis. Considering the existing sedimentary and topographic loads, the isostatic analysis has shown that mass inhomogeneities below the CMI are needed to explain this gradient. The extinct spreading axis would then mark the separation between lower densities in the northwest and higher density in the southeast. This could be an indication of asymmetry below the CMI, at mantle level, as was found in the MELT experiment.

[28] The magmatic source of the spreading axis and of the subsequent Cenozoic volcanic activity which affected east

Asia and the South China Sea Basin has been matter of some debate. The occurrence of DUPAL isotopic signature (high $^{207}\text{Pb}/^{204}\text{Pb}$, $^{208}\text{Pb}/^{204}\text{Pb}$ and $^{87}\text{Sr}/^{86}\text{Sr}$ ratios [Hart, 1984]) in Cenozoic intraplate and marginal basin basalts (South China Sea and Sea of Japan) in Asia led to the interpretation of the presence of several hot spots [Deng *et al.*, 1998]. In particular the presence of three plumes was postulated for the east Asia continental margin, the southernmost of which would be responsible for the Cenozoic volcanism of South China and Vietnam and the spreading of the South China Sea [Deng *et al.*, 1998]. Alternatively the volcanism was produced by the presence of asthenospheric convection cells induced by topographic variation at the continental mantle-asthenosphere boundary and interactions of the China, Pacific and Indian plates [Smith, 1998]. Tu *et al.* [1992] propose that the isotopic compositions of the South China Basin volcanism reflect mantle sources which comprise both asthenospheric and lithospheric components, including a lower region of accreted asthenospheric melt overprinted by radiogenic melts of subducted sediments. The existence of a plume beneath Hainan has been proposed from *S* velocity tomography, maybe reaching the transition zone (410–660 km depth) by Lebedev and Nolet [2003]. At shallower depth the low-velocity zone is broader, and is found beneath Vietnam up to 350 km depth and below the South China Sea up to 150 km depth. The presence of a mantle plume alone is not sufficient to explain all the different expressions of volcanism. The South China Sea spreading continued between 32 and 15 Ma, after which the Cenozoic volcanism started on Hainan and South Vietnam [Lee *et al.*, 1998; Tu *et al.*, 1992] and continued until modern times. The seamounts in South China Sea were emplaced after spreading ceased, until 0.5 Ma [Su *et al.*, 1989; Tu *et al.*, 1992]. The timing and geographical distribution of the different volcanic activities does not fit a model in which a geographical migration of volcanic activity is due to plate movement above a fixed hot spot, as the more recent activity is geographically disjunct and covers a larger area than the deep subvertical low-velocity zone interpreted as the plume below Hainan. Our study has shown that the southwestern subbasin has a well developed central axis. We have also found that the southwestern subbasin is devoid of seamounts, which gives evidence of the fact that the volcanic activity shifted from this subbasin back to the northwestern China Sea basin and the surrounding areas after spreading ceased.

[29] **Acknowledgments.** We acknowledge support from the Italian CNR and Chinese CAS, in particular, in the frame of the Italian-Chinese exchange program between the University of Trieste and the Institute of Geodesy and Geophysics, CAS, in Wuhan. Susann Wienecke profited from a Socrates student exchange program and from a Vigoni exchange program between the University of Trieste and the Freie Universität Berlin (Resp. in Berlin H. J. Götze). Peter Clift in particular and an anonymous reviewer are thanked for valuable suggestions; Tim Redfield is thanked for revising the English.

References

- Bassin, C., G. Laske, and G. Masters (2000), The current limits of resolution for surface wave tomography in North America, *Eos Trans. AGU*, 81(48), Fall Meet. Suppl., Abstract S12A-03.
- Bellingham, P., and N. White (2000), A general inverse method for modeling extensional sedimentary basins, *Basin Res.*, 12, 219–226.
- Blakely, R. J. (1995), *Potential Theory in Gravity and Magnetic Applications*, 441 pp., Cambridge Univ. Press, New York.
- Braitenberg, C., and M. Zadro (1999), Iterative 3D gravity inversion with integration of seismicologic data, *Bol. Geofis. Teor. Appl.*, 40(3–4), 469–476.
- Braitenberg, C., F. Pettenati, and M. Zadro (1997), Spectral and classical methods in the evaluation of Moho undulations from gravity data: The NE Italian Alps and isostasy, *J. Geodyn.*, 23, 5–22.
- Braitenberg, C., M. Zadro, J. Fang, Y. Wang, and H. T. Hsu (2000), The gravity and isostatic Moho undulations in Qinghai-Tibet plateau, *J. Geodyn.*, 30(5), 489–505.
- Braitenberg, C., J. Ebbing, and H.-J. Götze (2002), Inverse modelling of elastic thickness by convolution method: The Eastern Alps as a case example, *Earth Planet. Sci. Lett.*, 202, 387–404.
- Braitenberg, C., Y. Wang, J. Fang, and H. T. Hsu (2003), Spatial variations of flexure parameters over the Tibet-Qinghai plateau, *Earth Planet. Sci. Lett.*, 205, 211–224.
- Braitenberg, C., E. Pagot, Y. Wang, and J. Fang (2004), Bathymetry and crustal thickness variations from gravity inversion and flexural isostasy, in *Satellite Altimetry for Geodesy, Geophysics and Oceanography*, edited by C. Hwang *et al.*, pp. 143–149, Springer, New York.
- Briaies, A., P. Patriat, and P. Tapponnier (1993), Updated interpretation of magnetic anomalies and seafloor spreading stages in the South China Sea: Implications for the tertiary tectonics of Southeast Asia, *J. Geophys. Res.*, 98, 6299–6328.
- Calmant, S., and N. Baudry (1996), Modelling bathymetry by inverting satellite altimetry data: A review, *Mar. Geophys. Res.*, 18, 123–134.
- Clift, P., and J. Lin (2001), Preferential mantle lithospheric extension under the South China margin, *Mar. Pet. Geol.*, 18, 929–945.
- Clift, P., J. Lin, and U. Barckhausen (2002), Evidence of low flexural rigidity and low viscosity lower continental crust during the continental break-up in the South China Sea, *Mar. Pet. Geol.*, 19, 951–970.
- Deng, J., H. Zhao, Z. Luo, Z. Guo, and X. Mo (1998), Mantle plumes and lithosphere motion in east Asia, in *Mantle Dynamics and Plate Interactions in East Asia*, *Geodyn. Ser.*, vol. 27, edited by M. F. J. Flower *et al.*, pp. 59–66, AGU, Washington, D. C.
- Ebbing, J., C. Braitenberg, and H.-J. Götze (2001), Forward and inverse modelling of gravity revealing insight into crustal structures of the Eastern Alps, *Tectonophysics*, 337, 191–208.
- Ebbing, J., C. Braitenberg, and H.-J. Götze (2006), The lithospheric density structure of the Eastern Alps, *Tectonophysics*, 414, 145–155.
- Forsyth, D. W., *et al.* (1998), Imaging the deep seismic structure beneath a mid-ocean ridge: The MELT experiment, *Science*, 280, 1215–1218.
- Hart, S. R. (1984), A large-scale isotope anomaly in the Southern Hemisphere mantle, *Nature*, 309, 753–757.
- Hwang, C. (1999), A bathymetric model for the South China Sea from satellite altimetry and depth data, *Mar. Geod.*, 22, 37–51.
- Hwang, C., E.-C. Kao, and B. Parsons (1998), Global derivation of marine gravity anomalies from Seasat, Geosat, ERS-1 and TOPEX/POSEIDON altimeter data, *Geophys. J. Int.*, 134, 449–459.
- Hwang, C., H.-Y. Hsu, and R.-J. Jang (2002), Global mean sea surface and marine gravity anomaly from multi-satellite altimetry: Applications of deflection-geoid and inverse Vening Meinesz formulae, *J. Geod.*, 76, 407–418.
- Hwang, C., H.-Y. Hsu, and X. Deng (2004), Marine gravity anomaly from satellite altimetry: A comparison of methods over shallow waters, in *Satellite Altimetry for Geodesy, Geophysics and Oceanography*, edited by C. Hwang *et al.*, pp. 59–66, Springer, New York.
- Intergovernmental Oceanographic Commission, International Hydrographic Organization, and British Oceanographic Data Centre (IOC, IHO, and BODC) (2003), *Centenary Edition of the GEBCO Digital Atlas on Behalf of the Intergovernmental Oceanographic Commission and the International Hydrographic Organization as Part of the General Bathymetric Chart of the Oceans*, [CD-ROM], Liverpool, U. K.
- Kearey, P., and F. J. Vine (1996), *Global Tectonics*, 2nd ed., 333 pp., Blackwell Sci., Malden, Mass.
- Kuszniir, N. J., G. Marsden, and S. S. Egan (1991) A flexural cantilever simple shear/pure shear model of continental extension, in *The Geometry of Normal Faults*, edited by A. M. Roberts *et al.*, *Spec. Publ. Geol. Soc. London*, 56, 41–61.
- Lallemant, S., Y. Font, H. Bijwaard, and H. Kao (2001), New insights on 3-D plates interaction near Taiwan from tomographic and tectonic implications, *Tectonophysics*, 335, 229–253.
- Lebedev, S., and G. Nolet (2003), Upper mantle beneath Southeast Asia from S velocity tomography, *J. Geophys. Res.*, 108(B1), 2048, doi:10.1029/2000JB000073.
- Lee, T.-Y., C.-H. Lo, S.-L. Chung, C.-Y. Chen, P.-L. Wang, W.-P. Lin, H. Nguyen, T. C. Cung, and T. Y. Nguyen (1998), $^{40}\text{Ar}/^{39}\text{Ar}$ dating result of Neogene basalts in Vietnam and its tectonic implication, in *Mantle Dynamics and Plate Interactions in East Asia*, *Geodyn. Ser.*, vol. 27, edited by M. F. J. Flower *et al.*, pp. 317–330, AGU, Washington, D. C.

- Lin, A. T., and A. B. Watts (2002), Origin of the West Taiwan basin by orogenic loading and flexure of a rifted continental margin, *J. Geophys. Res.*, 107(B9), 2185, doi:10.1029/2001JB000669.
- Ludwig, W. J., and R. E. Houtz (1979), Isopach map of the sediments in the Pacific Ocean basin, map with text, Am. Assoc. of Pet. Geol., Tulsa, Okla.
- Ministry of Geology and Mineral Resources (1992), Map series of geology and geophysics of China Sea and adjacent regions, Geol. Publ. House, China.
- Nissen, S. S., D. E. Hayes, B. Yao, W. Zeng, Y. Chen, and X. Nu (1995), Gravity, heat flow, and seismic constraints on the processes of crustal extension: Northern margin of the South China Sea, *J. Geophys. Res.*, 100, 22,447–22,483.
- Parker, R. L. (1972), The rapid calculation of potential anomalies, *Geophys. J. R. Astron. Soc.*, 31, 447–455.
- Ramillien, G., and A. Cazenave (1997), Global bathymetry derived from altimeter data of the ERS-1 geodetic mission, *J. Geodyn.*, 23, 129–149.
- Russo, R. M., and R. C. Speed (1994), Spectral analysis of gravity anomalies and the architecture of tectonic wedging, NE Venezuela and Trinidad, *Tectonics*, 13(2), 613–622.
- Sandwell, D. T., and W. H. F. Smith (2001), Bathymetric estimation, in *Satellite Altimetry and Earth Sciences*, edited by L.-L. Fu and A. Cazenave, pp. 441–457, Elsevier, New York.
- Sclater, J. G., and P. A. F. Christie (1980), Continental stretching: An explanation of the post mid-Cretaceous subsidence of the central North Sea basin, *J. Geophys. Res.*, 85, 3711–3739.
- Sibuet, J. C., S. K. Hsu, and E. Debayle (2004), Geodynamic context of the Taiwan orogen, in *Continent-Ocean Interactions in the East Asian Marginal Seas*, *Geophys. Monogr. Ser.*, vol. 149, edited by P. D. Clift et al., pp. 127–158, AGU, Washington, D. C.
- Smith, A. D. (1998), The geodynamic significance of the DUPAL anomaly in Asia, in *Mantle Dynamics and Plate Interactions in East Asia*, *Geodyn. Ser.*, vol. 27, edited by M. F. J. Flower et al., pp. 89–106, AGU, Washington, D. C.
- Smith, W. H. F., and D. T. Sandwell (1997), Global sea floor topography from satellite altimetry and ship depth soundings, *Science*, 277, 1956–1962.
- Spector, A., and F. S. Grant (1970), Statistical models for interpreting aeromagnetic data, *Geophysics*, 35, 293–302.
- Su, D., N. White, and D. McKenzie (1989), Extension and subsidence of the Pearl River mouth basin, northern South China Sea, *Basin Res.*, 2, 205–222.
- Taylor, B., and D. E. Hayes (1980), The tectonic evolution of the South China Sea basin, in *The Tectonic and Geologic Evolution of Southeast Asian Seas and Islands*, *Geophys. Monogr. Ser.*, vol. 23, edited by D. E. Hayes, pp. 89–104, AGU, Washington D. C.
- Taylor, B., and D. E. Hayes (1983), Origin and history of the South China Sea basin, in *The Tectonic and Geologic Evolution of Southeast Asian Seas and Islands: Part 2*, *Geophys. Monogr. Ser.*, vol. 27, edited by D. E. Hayes, pp. 23–56, AGU, Washington D. C.
- Tu, K., M. F. J. Flower, R. W. Carlson, G. Xie, C.-Y. Chen, and M. Zhang (1992), Magmatism in the South China basin. 1. Isotopic and trace-element evidence for an endogenous Dupal mantle component, *Chem. Geol.*, 97, 47–63.
- Wang, P., et al. (2000), *Proceedings of the Ocean Drilling Program: Initial Reports*, vol. 184, Ocean Drill. Program, College Station, Tex. (Available at http://www-odp.tamu.edu/publications/184_IR/184ir.htm.)
- Wang, Y., H. Xu, and J. Zhan (2001), High resolution bathymetry of China seas and their surroundings, *Chin. Sci. Bull.*, 46, 1661–1664.
- Wang, Z.-L., G.-S. Wu, and B. Chen (1997), *A Comprehensive Geophysical Study of the Basement Structure of the Zhujangkou Basin and the Shelf Basin of the East China Sea* (in Chinese), 97 pp., Tongji Univ., Shanghai, China.
- Watts, A. B. (2001), *Isostasy and Flexure of the Lithosphere*, 458 pp., Cambridge Univ. Press, New York.
- White, R. S. (1999), The lithosphere under stress, *Philos. Trans. R. Soc., Ser. A*, 357(1753), 901–915.
- Xu, D., et al. (1997), *China Offshore Geology*, pp. 247–252, Geol. Publ. House, Beijing.
- Zadro, M. (1986), Spectral images of the gravitational field, *Manuscr. Geod.*, 11, 207–213.
- Zadro, M., and C. Braitenberg (1997), Spectral methods in gravity inversion: The geopotential field and its derivatives, *Ann. Geofis.*, 40(5), 1433–1443.

C. Braitenberg, Department of Earth Sciences, Trieste University, Via Weiss 1, I-34100 Trieste, Italy. (berg@univ.trieste.it)

Y. Wang, Institute of Geodesy and Geophysics, Chinese Academy of Sciences, 54 Xu Dong Road, 430077 Wuhan, China.

S. Wienecke, NGU, N-7491 Trondheim, Norway.